Thermodynamic and Vertical Velocity Structure of Two Gust Fronts Observed with a Wind Profiler/RASS during MCTEX

PETER T. MAY

Bureau of Meteorology Research Centre, Melbourne, Australia

(Manuscript received 8 May 1998, in final form 28 August 1998)

ABSTRACT

High-time-resolution wind profiler/RASS observations are used to describe the vertical velocity, temperature, and reflectivity fields of two gust fronts in detail. The first was a freely propagating gust front and the second interacted with a rain cell near the profiler site. The first of these shows a large updraft confined to the warm air ahead of the front. This updraft coincided with the (nonhydrostatic) pressure jump. The vertical motions within the gust front were an order of magnitude smaller. The updraft impinging on the top of the boundary layer excited a clear gravity wave signature in the free troposphere. The interaction of the vertical circulation and the weakly precipitating cloud in the second case coincided with explosive growth of the cell with reflectivities increasing from ~30 dBZ to >50 dBZ in 6 min. A descending reflectivity core was observed at this time. Precipitation loading played a significant role in a downdraft behind the gust front head leading to adiabatic warming as no evidence of evaporative cooling in the downdraft was seen. A distinct clear air peak was visible in the profiler Doppler spectra even during the heavy rain.

1. Introduction

The kinematic structure of gust fronts and their interactions with the environment have been much studied using a variety of techniques including tower data (e.g., Charba 1974; Goff 1976), Doppler radar (e.g., Wilson and Schreiber 1986; Wakimoto 1982), and numerical modeling (Seitter 1986; Droegemeier and Wilhelmson 1985). Gust fronts are examples of gravity currents (e.g., Benjamin 1968; Simpson and Britter 1980). The basic gravity current dynamics occur across a wide range of atmospheric phenomena including cold fronts (e.g., Carbone 1982; Seitter and Muench 1985; Shapiro et al. 1985) and sea breezes (Simpson 1969). A recent study used a high temporal resolution vertically pointing X-band radar to directly measure the vertical velocity field in a gust front in the United States (Martner 1997).

There have been three main areas of focus in gust front studies. The first is the kinematic structure of the gust fronts and their evolution with time (e.g., Wakimoto 1982; Mueller and Carbone 1987), and the second is interactions between gust fronts and other boundaries that frequently result in the initiation of new convection (e.g., Knupp and Cotton 1982; Wilson and Schreiber 1986; Mahoney 1988; Droegemeier and Wilhelmson 1985). A third area of study has been the role of gust fronts and their relation with the low-level shear in maintaining long-lived convective systems (Thorpe et al. 1982; Rotunno et al. 1988). The kinematic description of gust fronts has centered around the description of gravity currents. Recent theoretical and modeling work has also examined the effects of the shear in the environmental flow on the gust fronts. Fronts opposing a mean flow develop a much steeper boundary with a larger head compared with those with a tailwind (Liu and Moncrieff 1996a). The interaction between the low-level shear and the gust front is crucial for the maintenance of erect updrafts in long-lived convective systems (Rotunno et al. 1988). Latent heat release results in a more slowly propagating system compared with an undisturbed gust front (Liu and Moncrieff 1996b).

Observational studies of the kinematic structure of gust fronts have been limited by the height of towers and the sampling limitations inherent with Doppler radar and aircraft measurements. During the Maritime Continent Thunderstorm Experiment (MCTEX; Keenan et al. 1994) large convective complexes formed on the islands every day of the experiment. Interactions between gust fronts and between gust fronts and sea-breeze fronts were crucial for the evolution of the storms (e.g., Carbone et al. 1997; Wilson et al. 1997). On two occasions, the wind profiler/Radio Acoustic Sounding System (RASS; May et al. 1990) at Maxwell Creek (Fig. 1) was switched from a routine wind and RASS measuring cycle to a continuous RASS measurement mode as gust fronts detected using the C-Pol Doppler radar

Corresponding author address: Dr. Peter T. May, BMRC, G.P.O. Box 1289K, Melbourne 3001, Victoria, Australia.
E-mail: p.may@bom.gov.au

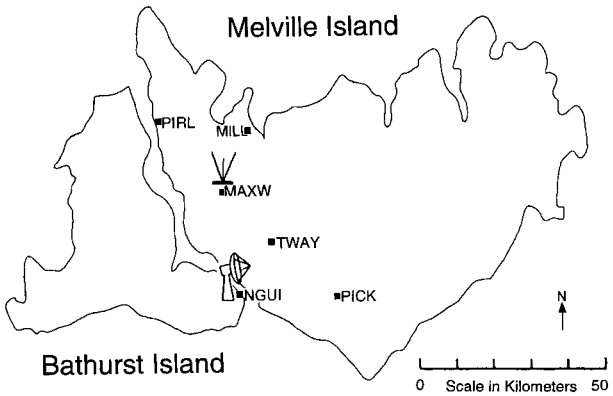

FIG. 1. The parts of the observational network deployed during MCTEX that were used in this study.

were approaching. High time (~23 s) and height (~100 m) resolution data of the virtual temperature, vertical motion, and radar reflectivity were combined with surface observations and Doppler radar data. These data enabled the kinematic aspects of the structure of the two gust fronts to be studied in detail with emphasis on the thermal structure and associated vertical velocity field.

The first event (20 November 1997) to be discussed was on a day when the convection was relatively suppressed, with low dewpoints. This delayed the onset of island convection; initiation was several hours later than was typical. However, the profiler data do show evidence of congestus penetrating the top of the mixed layer a short time prior to the arrival of the gust front. This gust front generated a well-defined rope cloud that persisted for more than an hour after the RASS observations as the gust front propagated off the island, but triggered no new convection. In the second event (30 November 1997) to be discussed, the gust front interacted with a weakly precipitating cloud near the profiler site. The cell developed rapidly as the gust front passed beneath with reflectivities reaching in excess of 50 dB*Z*. The profiler was near the edge of this cell and a distinct descending reflectivity core was observed. Cell and gust front circulations coexisted over the profiler.

2. Observational tools

There were three 920-MHz boundary layer wind profilers (Ecklund et al. 1990) deployed on Melville Island (~70 km north of Darwin) during MCTEX. The Maxwell Creek profiler was a commercial Radian system with 9° beamwidth and included a RASS capability.

For the periods of interest, the boundary layer wind profiler was operated in a continuous (vertically pointing) RASS mode with 100-m vertical resolution with data collected approximately every 23 s. In RASS, the ground relative speed of sound is measured using the radar backscatter from the density fluctuations of the sound wave (e.g., May et al. 1990). The airspeed is subtracted and the virtual temperature estimated from the speed of sound [$T_v = (C_a/20.047)^2$ K, where C_a is the speed of sound in still air in m s^{-1}]. Useable RASS data were obtained from a height of 100 m up to an altitude of approximately 1 km and clear air signals were collected up to 2 km allowing vertical velocity and reflectivity estimates. Horizontal winds were not estimated during the periods around the gust front in order to maximize the sampling rate of the vertical motion and virtual temperature fields. These data were supported by an automatic weather station (AWS) located about 200 m from the profiler. Profiles of potential virtual temperature (θ_v) were calculated using the surface and RASS observations with the pressure profile calculated by integrating the hydrostatic equation.

The vertical velocities measured by the profiler were recalculated to remove the effects of severe ground clutter that was encountered up to a height of about 900 m. The clutter was evident in the raw data, particularly on 20 November. A multitiered approach was used to obtain unbiased estimates. First, interpolation across three spectral points about zero velocity was applied and the spectral moments were estimated over a limited velocity and power range about the spectral peak. The spectra and velocity estimates were then examined and if clutter bias was still evident, an analysis using the interpolated spectrum, and a spectrum where the symmetric component about zero velocity was removed (Passarelli et al. 1981), was applied. This was done as a last resort for the worst affected cases, as it was manually intensive and the simple application of the symmetric removal results in estimates biased away from small velocities. The results and spectra were then manually inspected and edited.

In the 30 November data, there were strong precipitation echoes (>40 dB*Z* over the profiler) for part of the period of interest. However, a small clear air peak remained visible in the Doppler spectra. This is shown in Fig. 2, which will be discussed later in relation to the detailed gust front observations of this case (section 4). This ability to discern a clearly separate clear air peak in precipitation with a 920-MHz profiler is in contrast to the observations of Gossard (1988) where precipitation (mostly drizzle) completely obscured the clear air echo. In the case of the heavy tropical rain, the median drop size (and hence fall speed) is large (as shown by large differential reflectivity measured by the polarimetric Doppler radar). This apparently allows enough spectral separation that the two peaks are visible in the Doppler spectra for much of the rain event allowing both vertical wind and precipitation observations. Examples of the spectra are shown from the onset of rain through to when the reflectivity over the profiler was greater than 40 dB*Z*. The recalculated vertical velocity estimates were used to subtract the air motion from the speed of sound RASS observations.

The original radar reflectivity estimates (dBZ_e) are retained as the recalculated moment estimates have substantial biases in the power estimates. Clutter is pri-

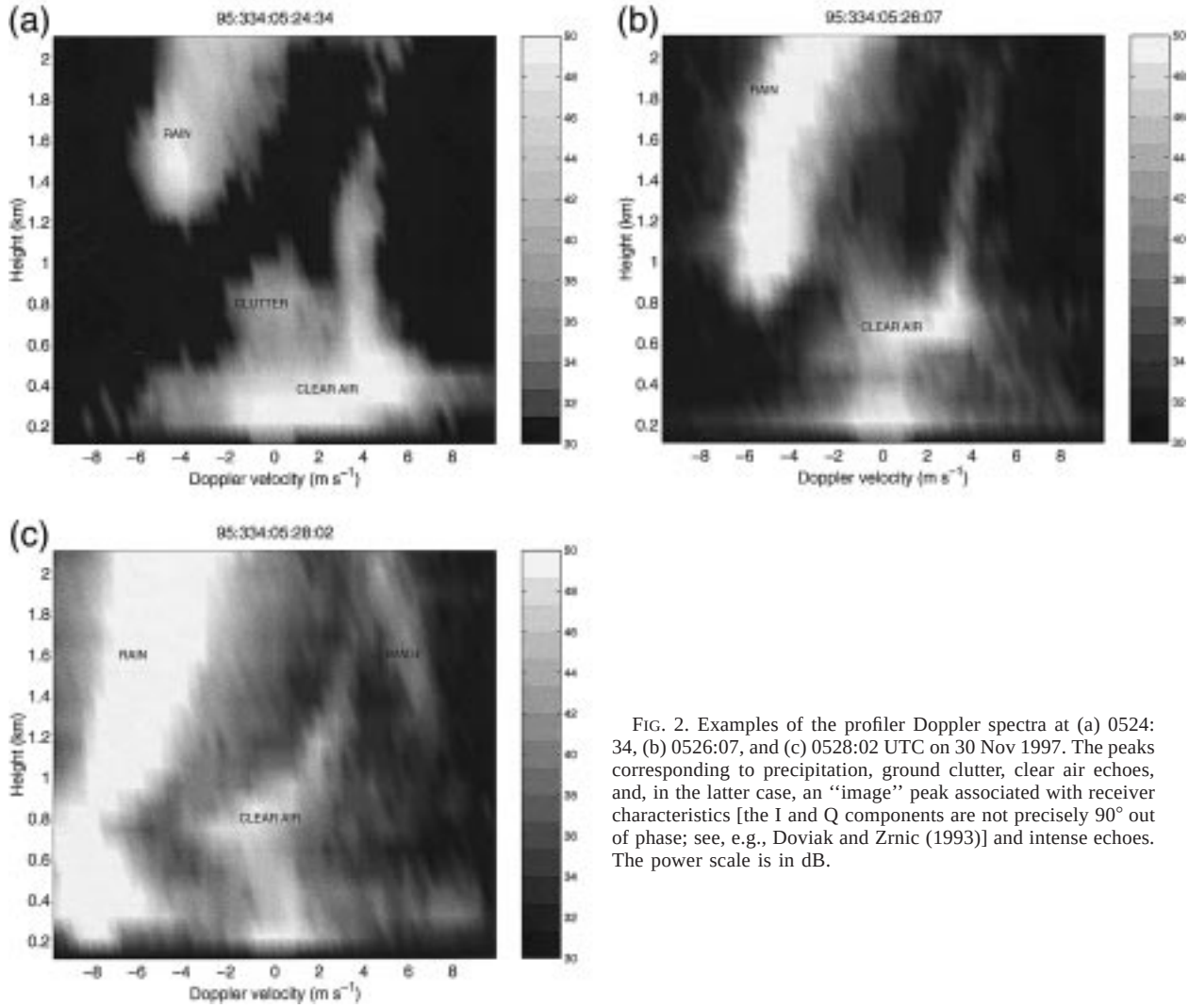

FIG. 2. Examples of the profiler Doppler spectra at (a) 0524:34, (b) 0526:07, and (c) 0528:02 UTC on 30 Nov 1997. The peaks corresponding to precipitation, ground clutter, clear air echoes, and, in the latter case, an ''image'' peak associated with receiver characteristics [the I and Q components are not precisely 90° out of phase; see, e.g., Doviak and Zrnic (1993)] and intense echoes. The power scale is in dB.

marily a problem at 200 m (both cases) and from 700–900 m on 20 November. In order to reduce the effect of the higher-elevation clutter in the 20 November data, the power at the affected upper heights has had a clutter component subtracted in the figures to be shown.

Doppler radar data from the 5-cm wavelength, 1° beamwidth C-Pol radar (Keenan et al. 1998) have also been used in this study. The radar was located approximately 25 km to the south of the profiler site giving it a resolution cell volume of 300 m in range by about 500 m in height. Clear air signals were easily detectable at this range throughout the day. During the periods of interest, the radar was used to conduct sector scans with the profiler site near the center of the range of azimuths. The lowest tilt (0.7°) will be used for the first case, while data from higher tilts has also been used in the analysis of the 30 November case where the gust front interacted with a convective cell over the profiler.

Data from various AWS sites on the Tiwi Islands and radiosondes launched from Maxwell Creek (Fig. 1) are used to supplement the RASS and Doppler radar data. Sondes were launched every 2 h during the period of interest.

3. The 20 November 1995 event

The first case to be discussed can be regarded as a pure gust front in that no new convection was being initiated as it propagated past the profiler. An 0600 UTC sounding shows the mixed layer 1650–1800 m deep. Profiler reflectivity time–height cross sections indicate that there was some penetration through the top of the mixed layer by nonprecipitating cumulus (not shown). However, there was no indication of deep convection forming near the profiler at this time.

A complex of cells developed on the northeastern part of Melville Island around 0400 UTC and moved westward, basically locked to the sea-breeze convergence

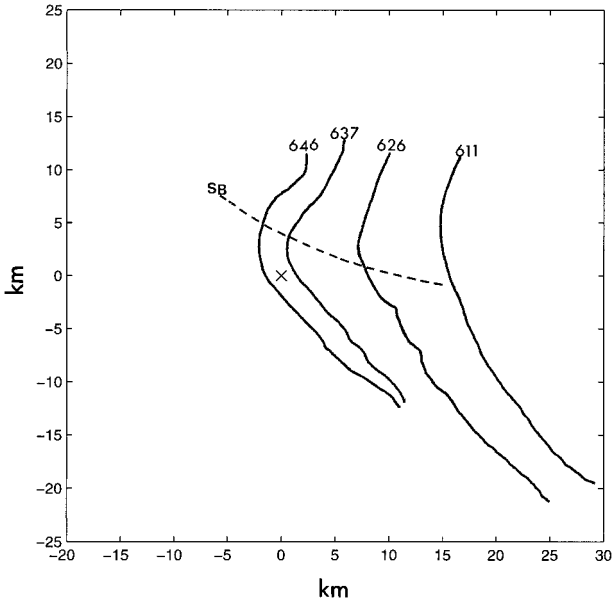

FIG. 3. Isochrone analysis of the radar fine line associated with the 20 Nov gust front. Also marked is the sea-breeze line at 0611 UTC.

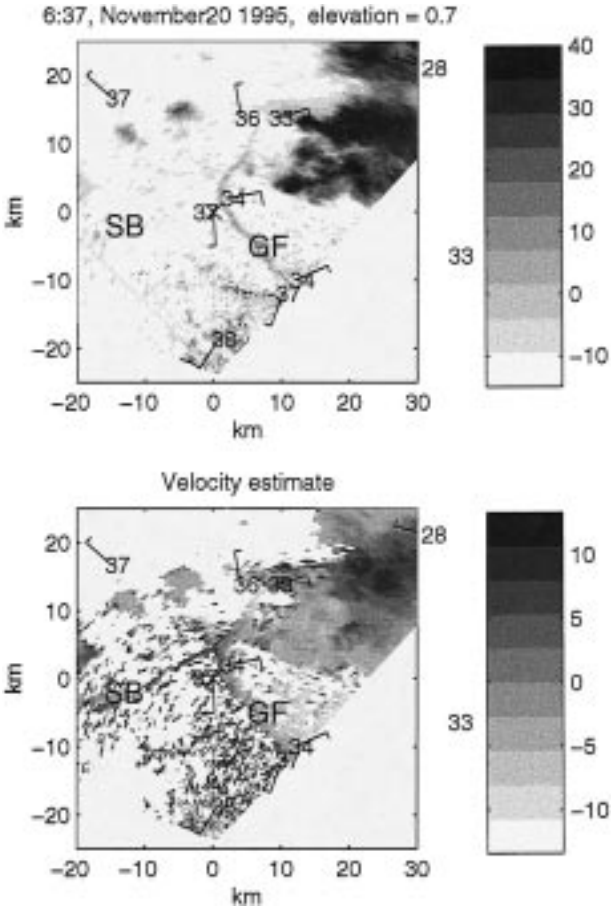

FIG. 4. Doppler radar measurements of reflectivity (upper) and radial velocity (lower) at an elevation of 0.7° at 0637 UTC 20 Nov 1995. The coordinate system is profiler relative, with the profiler located at the X. AWS measurements of wind (barb = 5 m s^{-1}, half barb = 2.5 m s^{-1}) and virtual temperature (°C) are shown. Measurements at sites close to the gust front are shown 5 min before and after the gust front passage with the positions on the display offset. Other AWS measurements were at 0637 UTC. The label GF marks the gust front fine line.

line. The movement was associated with an easterly steering flow and new development near the intersection of storm outflow and the sea breeze (Wilson et al. 1997). A well-defined gust front outflow from the complex was formed just prior to 0600 UTC and propagated to the south and west toward the profiler. An isochrone analysis of the radar fine line associated with the gust front is shown in Fig. 3 along with the position of the sea-breeze front propagating from the northern coast at 0611 UTC. There was considerable curvature of the gust front near the intersection with the sea breeze. A radar fine line associated with the sea breeze was still visible at 0637 UTC (best seen in the velocity data; Fig. 4) intersecting the gust front just to the north of Maxwell Creek. Figure 4 is a C-Pol image that shows the gust front fine lines and associated sea breeze with the parent complex to the northeast. The reflectivity scale has been chosen to highlight the gust front. Cells with reflectivity greater than 50 dBZ were embedded in the complex. Surface winds and virtual temperature at the time are also shown. AWS data near the fine line include data from just prior (~5 min before and after the gust front arrival in the AWS time series) to the gust front passage determined from the original time series. The gust front was moving at 6 m s^{-1} and was interacting with a sea-breeze boundary just to the north of the profiler site (Figs. 3, 4). The extension of the fine line to the south indicates that the speed of propagation north of the sea-breeze line was slower than to the south by 1–2 m s^{-1}. Note that this effect is exaggerated in Fig. 4 because the storms were advecting westward following the gust front. The speed difference is because of a significantly stronger head wind component and a slightly smaller temperature contrast between the gust front air and the sea-breeze air compared with the unmodified ''island'' air, although by this time the sea-breeze–island air temperature contrast was small. The reflectivity of the fine line was also reduced to the north of the sea-breeze intersection. By the time the gust front reached the profiler site at 0646 UTC, it was in a mature state with weak rear-to-front flow evident within the cold air (Wakimoto 1982). The gust front continued to move away from the islands, with a rope cloud visible offshore in satellite images.

Time–height cross sections of the (wind profiler derived) radar reflectivity, vertical velocity, and potential virtual temperature (θ_v) are shown in Fig. 5 and clearly illustrate the gust front passage. Time series of the surface observations and the virtual temperature at a height of 300 m and vertical velocity at a height of 200 m are shown in Figs. 6a–c. A five-point median filter has been

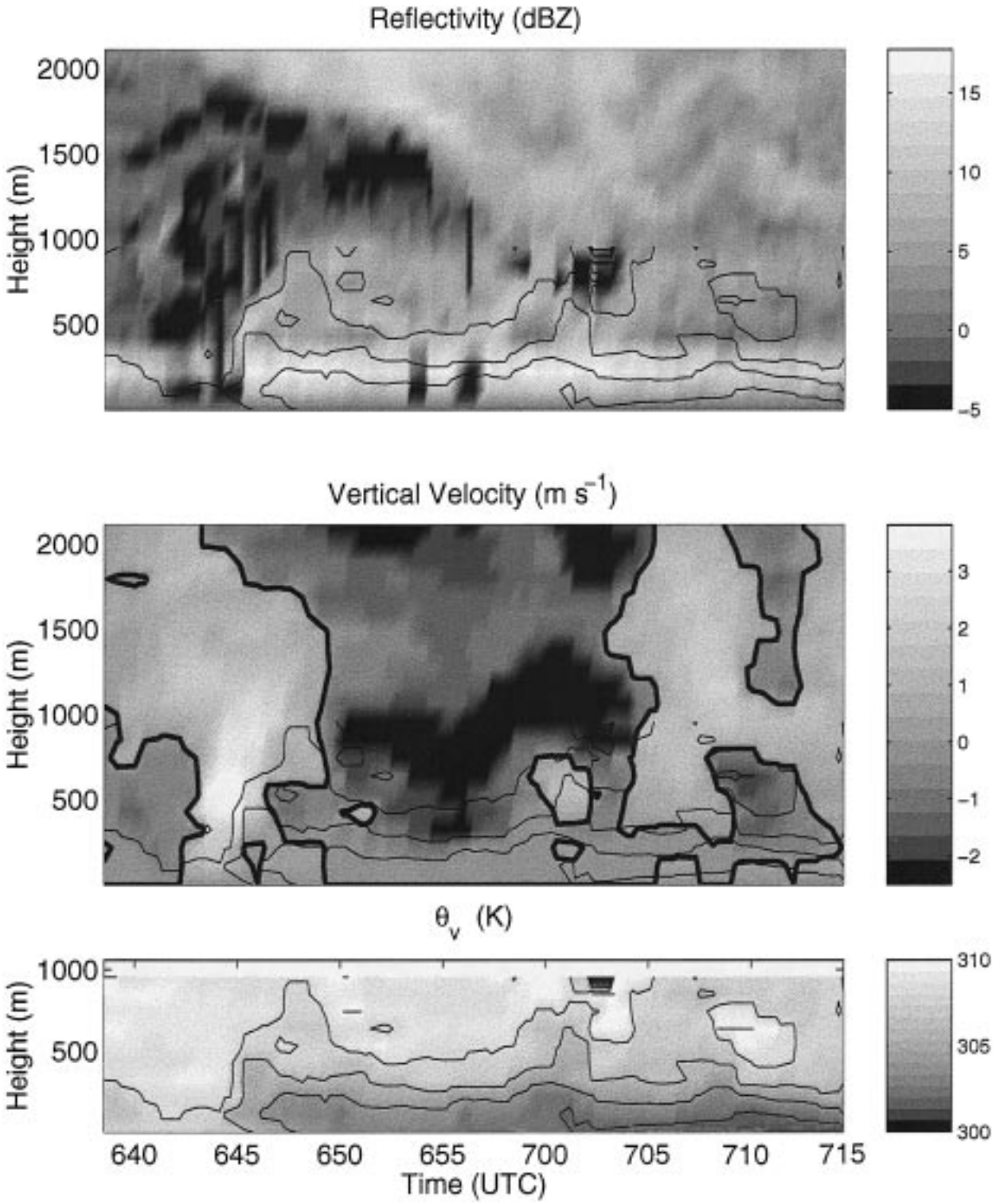

FIG. 5. Time–height cross sections of the radar reflectivity in dBZ_e (upper), vertical velocity (m s^{-1}, center), and potential virtual temperature (K, lower) during the passage of the 20 Nov gust front. Contours of the θ_v time–height sections overlay the three panels. The heavy contour on the center panel marks the 0 m s^{-1} isotach. The profiler temperature and velocity time series have been passed through a five-point median filter.

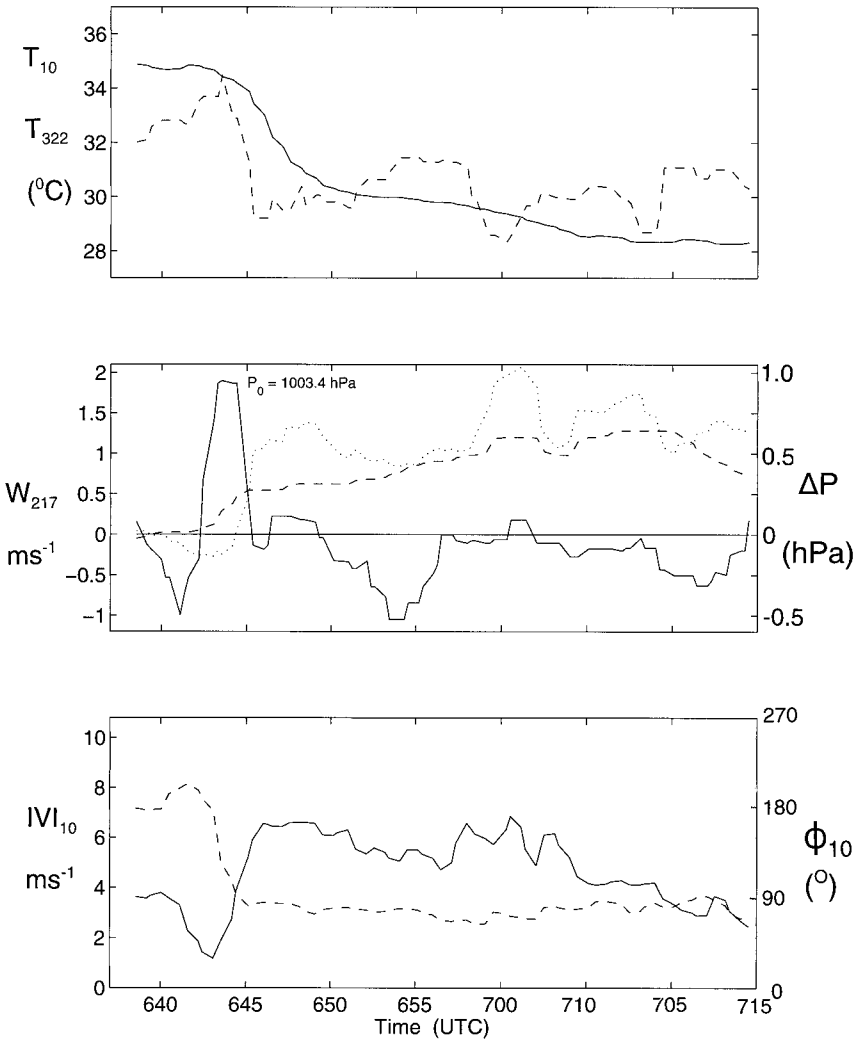

FIG. 6. Time series of (a) temperature at 10 m (solid) and 322 m (dashed), (b) vertical motion at 217 m (solid), surface pressure perturbation (dashed) and calculated hydrostatic pressure perturbation (dotted), and (c) surface wind speed (solid) and direction (dashed). The pressure perturbations are calculated from a reference comprising the median pressure during the first 3 min of the record given on the left-hand side of the pressure trace. The hydrostatic pressure perturbation is estimated by integrating the hydrostatic equation up to 800 m using the surface and RASS virtual temperature data.

passed through the data to remove noise in the time series. Note that a median filter preserves sharp transitions that persist for longer than the filter length.

The air motion ahead of the front was weak, with general downward motion, and the θ_v profiles are well mixed (Fig. 5). There were relatively strong upward motions beginning at 0642 UTC and persisting for about 2 min. The maximum upward motion was in excess of 4 m s^{-1} but weakened dramatically at the top of the mixed layer ($\sim$1.5 km). The upward motion near the leading edge coincided with a period of a rapid rise in surface pressure that occurred solely within the warm air. That is, the cold air arrived at the rear of the upward motion and all the strong ascent was confined to the warm air. The sharp pressure rise had ceased by this time (Fig. 6). Thus the pressure rise coincided with the vertical acceleration rather than the arrival of the cold air confirming its nonhydrostatic origin (Wakimoto 1982). The surface wind speed dropped prior to the pressure jump and sharply increased into the cold air consistent with a response to the pressure perturbation.

There was significant descent immediately behind the head, as expected for relative flow up and over the gust front head. This is consistent with modeling for the case where the low-level shear across the depth of the cold pool is much less than the speed of the gust front propagation (cf. Rotunno et al. 1988), as was the case here. The fact that the gust front was propagating away from

the parent convection demonstrates that the shear and gravity current velocity are well away from the Rotunno et al. optimum state for erect circulations tied to convection.

A distinct head structure about 700 m deep was observed in both the reflectivity and θ_v sections (Fig. 5) as expected for the case where the gust front motion is opposing the environmental flow (Liu and Moncrieff 1996a). Doppler radar data as well as the surface winds all indicate that any rear-to-front flow within the body of the cold outflow was weak, at most 1–2 m s^{-1}. This is supported by the weak vertical motions within the head. There are some small vertical velocity oscillations within the head with upward motion of $\sim$20 cm s^{-1} below 400 m and descent above this (not shown). The cold air boundary was also marked by an increase in radar reflectivity. The effective reflectivity of the enhancement was similar to the C-band data indicating that the enhanced reflectivity was associated with Rayleigh scatterers, probably insects, even at a frequency of 920 MHz. The temperature drop above 100 m was much sharper than the temperature drop near the surface.

The main body of cold air was about 400 m deep and 5°–6°C colder than the environmental air (Fig. 5). Above this, mixing appeared to be occurring within a 200-m-deep layer. There were some undulations in the depth of the cold air. The first of these, at 0701 UTC, was accompanied by another pressure increase, a further drop in temperature, an increase in wind speed, and upward motion in the cold air. The bulge in the cold air is also clearly seen in the reflectivity field. The second undulation was associated with a similar increase in wind speed and pressure. Figure 6 shows both the observed pressure rise and the relative contribution from the calculation of the hydrostatic pressure change due to changes in the temperature profile below 800 m. This shows the hydrostatic contribution to the pressure increasing after the nonhydrostatic jump and reaching a value similar to the observed pressure changes. However, the hydrostatic pressure rise associated with the head of the gust front and the surges was greater than, but coincident with, the actual observed pressure jumps.

Between 0650 and 0705 UTC there were large-amplitude downward motions above the cold air (Fig. 5, center panel). An initial hypothesis that these downward motions were associated with biases in the profiler estimates induced by precipitation has been ruled out by the weak reflectivity and the fact that the profiler Doppler spectra showed no sign of anything other than a clear air signature. Visual observations on site recorded only upper-level anvil clouds at this time.

An extensive wavelike signature with a period of about 10 min (similar to the Brunt–Väisälä frequency in the free troposphere) is seen in the reflectivity field above the mixed layer trailing behind the leading edge (Fig. 5, top panel). This is almost certainly a response from deceleration of the updraft at the leading edge as it impinged on the top of the boundary layer. The lower boundary visible in the wave signature probably represents oscillations in the boundary layer–free troposphere boundary. This wave has vertical motions with an amplitude in excess of 2 m s^{-1} with considerable vertical extent. It is tempting to speculate that such waves may be responsible for initiating convection well after a gust front passage. Evidence for waves trailing the gust front has also been seen in Doppler radar analyses (Weckworth and Wakimoto 1992). This theory may also explain the frequent observations of large-amplitude internal waves with a frequency near the Brunt–Väisälä frequency that are observed through the midtroposphere some distance away from active convective systems in the Tropics (May et al. 1995).

The downward motions in the mixed layer are probably a response to the gravity wave vertical motions at the top of the mixed layer. The fluctuations are certainly in phase and the response is analogous to the convection wave observations of Kuettner et al. (1987).

The speed of gravity currents has been extensively studied (e.g., Benjamin 1968). The densimetric speed of a current c is given by

$$c = k(gh\Delta\theta_v/\theta_v)^{1/2} - 0.7u,$$

where k is the Froude number [theoretically equal to $\sqrt{2}$, but, observationally, values of about 0.7 give better agreement with atmospheric flows; Wakimoto (1982)], g is the acceleration due to gravity, $\Delta\theta_v$ is the virtual potential temperature contrast between the environment and the gravity current air, θ_v is the virtual potential temperature of the environment, h is the depth of the head, and the correction for the mean flow opposing the gravity current movement (u) is due to Simpson and Britter (1980). There are several similar equations for estimating the densimetric speed (e.g., Carbone 1982). For example the replacement of h by an estimate of twice the depth of the cold air in the flow following the head is more robust in many cases (Carbone et al. 1990; Seitter 1986) and has been used here. The greatest uncertainty is for the value of the Froude number where values between 0.7 and 1 have been widely produced in the literature. In fact, it is the uncertainty in k that dominates the error estimates followed by the uncertainty in the depth. For this case, the densimetric speed is 9 ± 2 m s^{-1}, somewhat larger than the observed velocity.

The structure of the cold air circulation also shows some differences with the classic gravity current circulation. There appears to be very little vertical motion within the cold air, except at the secondary surges and the flow within the cold air is simply advection, rather than the rear-to-front flow with overturning in gravity current models and a very weak rotor within the head. There is a distinct turbulent zone at the top of the gravity current (cf. Mueller and Carbone 1987). If we assume that the surface winds within the gust front are similar to the wind near the top part of the gust front, and the surface wind prior to the gust front arrival is similar to

the wind above the turbulent zone, we can calculate the Richardson number:

$$\mathrm{Ri} = (g/\theta)(\Delta\theta/\Delta z)(\Delta u/\Delta z)^{-2},$$

where Δz is the thickness of the transition zone at the top of the layer and Δu is the wind shear across the layer. Using the available data and for $\Delta z \approx 200$ m the Ri is equal to 0.79 and presumably smaller values existed on small scales (allowing Kelvin–Helmholtz instability and turbulent breakdown), similar to the results obtained by Mueller and Carbone (1987) and Weckworth and Wakimoto (1992). This is sufficient to maintain Kelvin–Helmholtz billows but these were not resolved; they may have been masked by the ground clutter contamination near the top of the gust front layer. It is also worth noting that the shear vector was not perpendicular to the gust front.

4. The 30 November 1995 event

The second gust front to be examined occurred on a more active day. A cell developed rapidly near the profiler as the gust front passed, so the profiler measurements show a combination of gust front and convective circulations.

The pre–gust front sounding (0400 UTC) showed a mixed layer depth of 1300–1500 m with little vertical shear of the horizontal wind above the surface layer. The low-level wind was northerly at 3 m s^{-1}, with stronger easterlies overlying the mixed layer leading to early development on the southern side of the islands (Carbone et al. 1997). By 0500 UTC an extensive east–west-oriented complex had formed along the south coast. The soundings were slightly more moist than the 20 November case with less convective inhibition evident.

A gust front propagating northward formed about 0500 UTC from convection along the southern coast of the islands (Fig. 7). The radar fine line signature of this gust front was shallower than the previous example (visible only in the lowest elevation, despite being less than 20 km from the radar) and had weaker clear air signals in the Doppler radar data. However, as noted, it was on a more convectively active day. At 0516 UTC there were some areas of weak precipitation just to the northwest of the profiler site and a weak cell with a maximum reflectivity of about 25 dBZ, at a height of about 2 km, that was slowly intensifying near the profiler site (Fig. 8a). At 0523 UTC, a region of enhanced reflectivity ($\sim$15 dBZ) was developing on the gust front, but it was still shallow (not shown). The developing cell had reached an intensity of about 32 dBZ at a height of 2 km by this time. An enhancement in the gust front outflow is evident at this location in the Doppler radar data. As the gust front arrived over the profiler (intersecting the cell), the cell rapidly intensified reaching a maximum reflectivity of over 50 dBZ within 6 min of the gust front passage (Fig. 8b). Successive radar observations show a descending reflectivity core with the cell

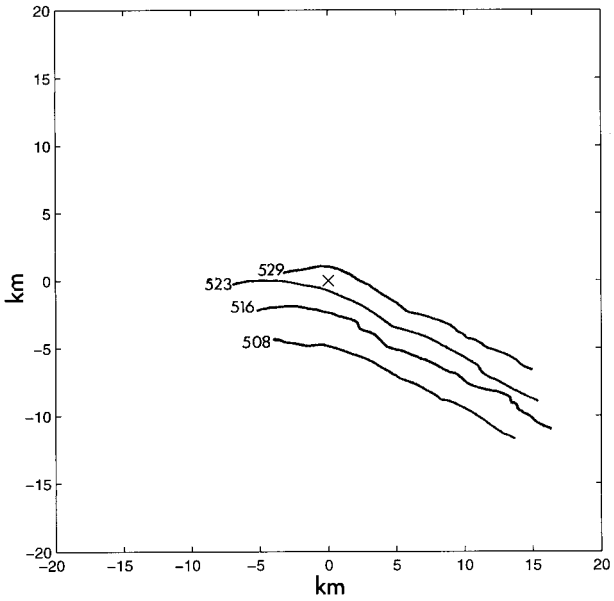

FIG. 7. Isochrone analysis of the radar fine line associated with the 30 Nov gust front.

moving slowly westward. The confluence across the gust front was greater than 10 m s^{-1} across a range of 300 m at a height of about 500 m, and extended up to over 1 km in altitude, easily sufficient to support the observed updrafts to be discussed next. The densimetric speed of the gust front was 4–7 m s^{-1}, similar to the speed estimated from the isochrone analysis ($c \sim 6$ m s^{-1}).

Three examples of stacked Doppler spectra measured by the profiler during the passage of the gust front are shown in Fig. 2 to illustrate the sharp boundary of the updraft associated with the gust front and the clear air signatures in the presence of rain. The top of the cold air is marked by a dramatic change in velocity within a single range gate. In Fig. 2a the precipitation echo only appears at the upper heights while it reaches down to below 1 km in Fig. 2b. By 0528 UTC (Fig. 2c), the precipitation echo intensity has increased over 10-fold and extends to near the surface. The profiler is most sensitive to the largest drops (reflectivity of a drop $Z \propto$ diameter D^6 for Rayleigh scatter), but the high fall speeds are an indication of a significant number of large drops (e.g., Foote and du Toit 1969), a fact supported by the high values of differential reflectivity ($Z_{DR} > 4$ dB) observed in this cell with the polarimetric radar. The velocity offset of the precipitation peak from the clear air peak is almost constant with height. Therefore the height variations of the vertical velocity field are reflected in the position of the rain echo peak as a function of height. In particular the shift to downward velocities is seen as the rain peak fall speed reaches 10 m s^{-1}. This latter example (Fig. 2c) also shows contamination of the spectra by an ''image'' peak associated with intense echoes and receiver characteristics. The

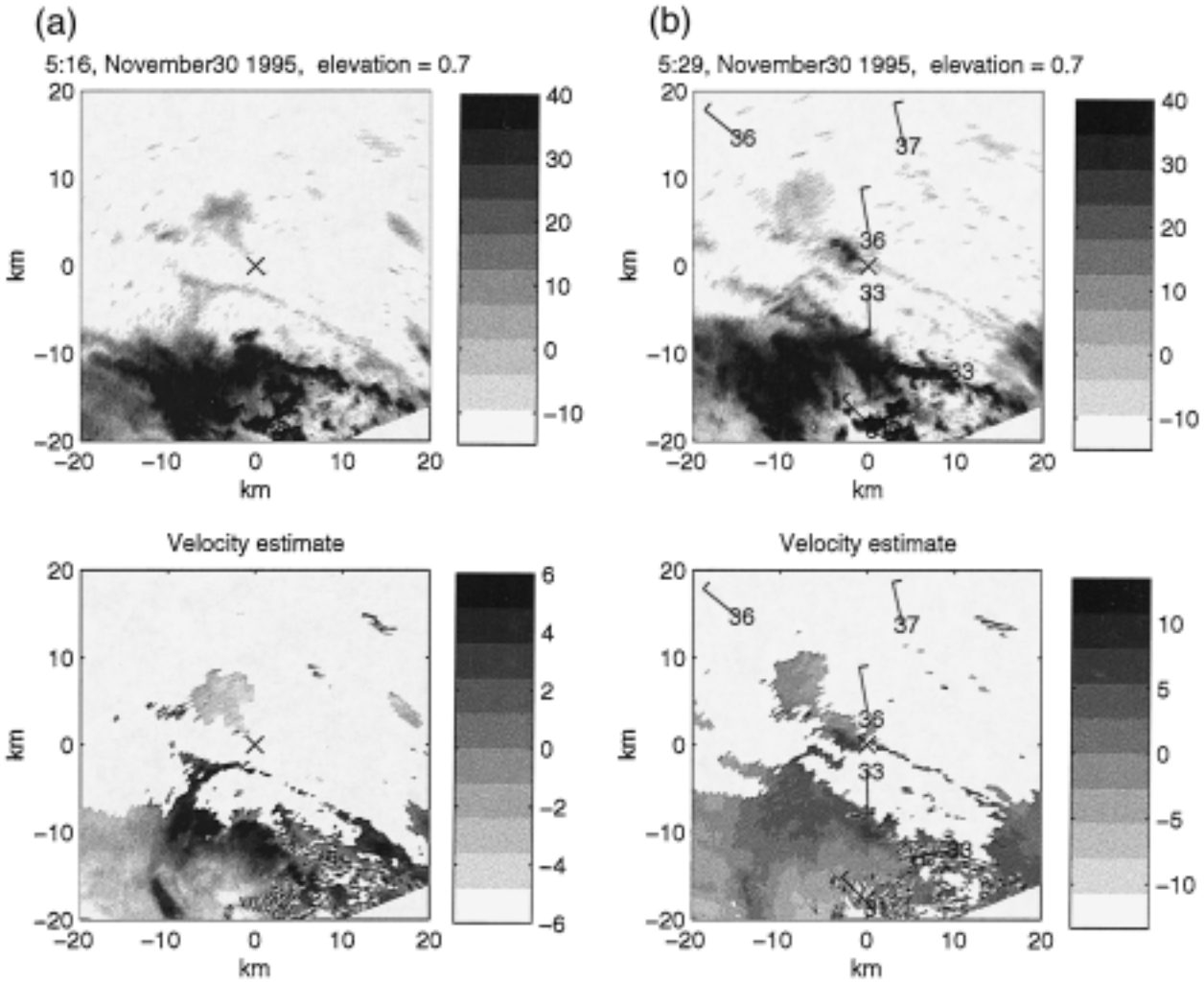

FIG. 8. As in Fig. 4 but for (upper) 0516 UTC and (lower) 0529 UTC 30 Nov 1995. The surface wind and virtual temperatures for 0529 UTC are shown in (b).

westward movement of the rain cell away from the profiler supports the inference that we are seeing a descending core, rather than the decrease in height of the rain peak with time, as the result of a rain cell being advected over the profiler site. Successive volumetric scans of C-Pol radar also show the height of maximum reflectivity decreasing with time.

Time–height cross sections of the profiler/RASS observations of radar reflectivity, vertical velocity, and potential virtual temperature are shown in Fig. 9. In this case the front was approaching a region of weak ascending motion in the boundary layer. Large upward motions were again seen in the warm air ahead of the leading edge of the cool air similar to the 20 November case. Again, the pressure rise corresponded to the upward acceleration and not the arrival of the cold air.

There was also a reflectivity maximum localized to the cold air interface (Fig. 9), as in the previous case. The head of the cold air was significantly deeper in the RASS observations in this case. As before, there were vertical velocity oscillations within the head, but in this case they were slightly larger than the previous case and upward on average. This is consistent with rear-to-front flow within the cold air as seen in the Doppler radar data in Fig. 8 where the velocity within the gust front exceeded the gust front propagation speed diagnosed from Fig. 7. Behind the head, the vertical motions within the cold air were again small.

There were a number of distinct features associated with the presence of the convective cell visible in Fig. 9. In addition to the gust front updraft, feeder flows both ahead and behind the main cell were seen. These feeder flows have vertical motions greater than 5 m s^{-1} and apparently exceed the magnitude of the vertical motions within the precipitation. Their origin was in the clear air at the edge of the cloud. The most intense convergence was seen in the lowest radar scan (elevation 0.7°, height ~500 m) across the gust front (Fig. 8b) and little

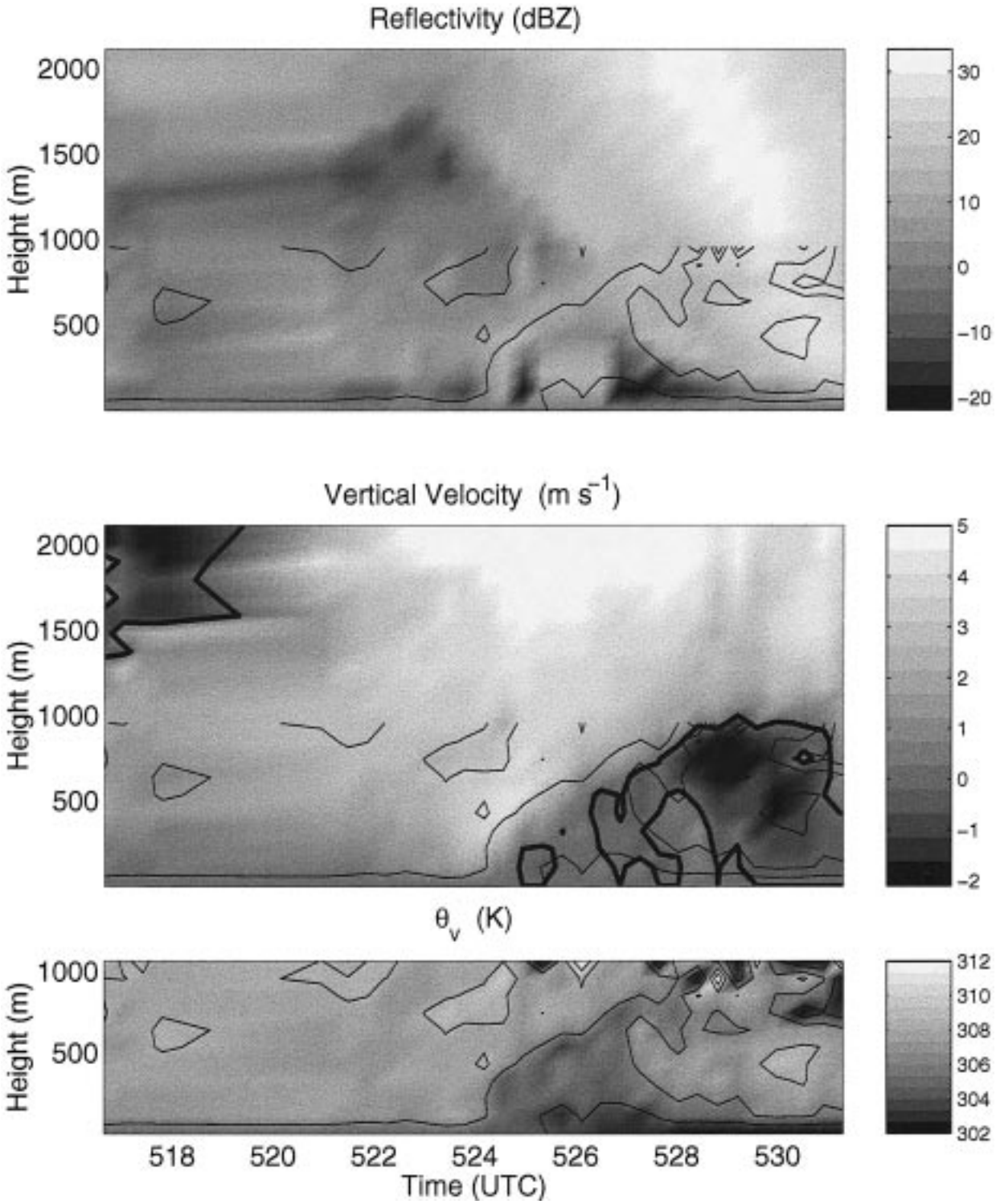

FIG. 9. As in Fig. 5 but for 30 Nov and with no filtering of the profiler data. During the rain period (seen as high reflectivity region descending with time) the clear air vertical motions were estimated using offline analysis.

convergence was seen in the next scan (2.2°, ~0.9 km). There was a stronger convergence signature in the third tilt (3.87°, ~1.6 km) data near the cloud edge (not shown). This is consistent with the low-level updraft associated with the gust front circulation and the separate feeder flow aloft observed with the profiler.

Figure 9 shows descending motion of greater than 1 m s^{-1} below a height of 1.2 km after 0528 UTC (behind the head) associated with the rapidly descending reflectivity core ($Z > 40$ dBZ). The precipitation loading associated with this is easily sufficient to support a downdraft in the well-mixed region but will not penetrate far across the gust front boundary with its large static stability. However, further support for descending motion in the lee of the head is expected as the shear was again much less than the propagation speed. Evaporation must be less important, as there is no evidence of cooling in the descending air. Note that the vertical displacement of the air parcels as they move over the profiler were less than or about 500 m ($w \sim 2$ m s^{-1} for 3 min), thus part of the warm air behind the cold dome is probably unmodified boundary layer air. The small changes in potential virtual temperature suggest some heating associated with adiabatic compression in the downdraft: indeed the θ_v's return to near the pre–gust front values as low as 200 m above the surface (recall the shallow nature of the radar gust front signature). This sequence of events illustrates the processes that may lead to a heat burst that has sometimes been observed in strong downdrafts (Johnson 1983; Johnson et al. 1989).

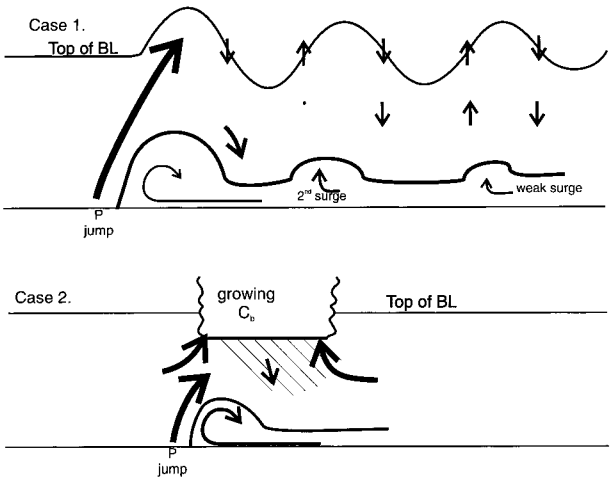

FIG. 10. Schematic outlining the gust front boundary and the top of the boundary layer along with the dominant vertical motions observed around the gust fronts.

5. Conclusions

The profiler/RASS data through the two gust fronts have been shown. The 6°C temperature drop is typical of tropical gust fronts. In comparison with studies of gust fronts over the Great Plains, these two examples appear to be shallower, but the degree of cooling across the gust front is comparable (e.g., Charba 1974; Mahoney 1988; Wakimoto 1982; Weckworth and Wakimoto 1992). This means that the propagation speeds and the associated pressure perturbations of these cases are somewhat less than the Great Plains cases. Figure 10 shows a schematic outlining the dominant features of the gust front circulations. The two datasets show many common features. A nonhydrostatic pressure jump associated with large-amplitude vertical motions in the warm air and the fine line reflectivity maximum on the cold air boundary was seen in both cases. The circulation shows some significant differences compared to the standard gravity current model. The rear-to-front flow in the first case (20 November) was relatively weak except in some secondary surges, although there is some indication of a rotor within the head in both cases. This may be a life cycle effect as both gust fronts were probably well into their ''mature'' phase when the rear-to-front flow is weakening and the cold air depth is becoming more shallow (Wakimoto 1982). While there was some evidence of a weak rotor within the head of the 30 November case, it is interesting that much larger updraft–downdraft couplets were observed around the head in the warm unmodified air in both cases, although the downdraft components may have contributions from different processes.

The 20 November case showed a remarkably clear gravity wave signature in both the radar reflectivity and vertical velocity field trailing behind the leading edge of the gust front. The velocity maxima were 90° out of phase with the maximum excursions in the reflectivity signature. The large-amplitude vertical motions induced by the wave within the mixed layer and above is a possible initiation mechanism for convection some time after a gust passage.

In the second case, an intense cell developed on the gust front. This was associated with an interaction between the gust front and a preexisting weak cell rather than being a pure response to the gravity current. Gust front signatures similar to the 20 November case were again observed, but with additional strong upward motion in feeder flows into the developing cell. A downdraft within the cold air with significant support from precipitation loading was also observed. There was little evidence of evaporative cooling being important in supporting the downdraft.

Acknowledgments. Part of this work was performed while the author was visiting the Cooperative Institute for Research in the Environmental Sciences, University of Colorado, supported by NASA Grant NAGW-4146. The author is indebted to Rob Schafer, Warner Ecklund, and Paul Johnson for their support of the profiler network during MCTEX. I gratefully acknowledge the insightful comments of Dr. R. E. Carbone and anonymous reviewers.

REFERENCES

Benjamin, T. B., 1968: Gravity currents and related phenomena. *J. Fluid Mech.,* **31,** 209–248.

Carbone, R. E., 1982: A severe frontal rainband. Part I: Stormwide hydrodynamic structure. *J. Atmos. Sci.,* **39,** 258–279.

——, J. W. Conway, N. A. Crook, and M. W. Moncrieff, 1990: The generation and propagation of a nocturnal squall line. Part I: Observations and implications for mesoscale predictability. *Mon. Wea. Rev.,* **118,** 26–49.

——, T. D. Keenan, J. W. Wilson, and J. M. Hacker, 1997: Boundary layer structures and the role of breezes in forcing deep island convection. Preprints, *28th Conf. on Radar Meteorology,* Austin, TX, Amer. Meteor. Soc., 565–566.

Charba, J., 1974: Application of gravity current model to analysis of squall-line gust front. *Mon. Wea. Rev.,* **102,** 140–156.

Doviak, R. J., and D. S. Zrnic, 1993: *Doppler Radar and Weather Observations.* 2d ed. Academic Press, 562 pp.

Droegemeier, K. K., and R. B. Wilhelmson, 1985: Three-dimensional numerical modeling of convection produced by interacting thunderstorm outflows. Part I: Control simulation and low level moisture variations. *J. Atmos. Sci.,* **42,** 2381–2403.

Ecklund, W. L., D. A. Carter, B. B. Balsley, P. E. Currier, J. L. Green, B. L. Weber, and K. S. Gage, 1990: Field tests of a lower tropospheric wind profiler. *Radio Sci.,* **25,** 899–906.

Foote, G. B., and P. S. du Toit, 1969: Terminal velocity of raindrops aloft. *J. Appl. Meteor.,* **8,** 249–253.

Goff, R. C., 1976: Vertical structure of thunderstorm outflows. *Mon. Wea. Rev.,* **104,** 1429–1440.

Gossard, E. E., 1988: Measuring drop-size distributions in clouds with clear-air sensing radar. *J. Atmos. Oceanic Technol.,* **5,** 640–649.

Johnson, B. C., 1983: The heat burst of 29 May 1976. *Mon. Wea. Rev.,* **111,** 1776–1792.

Johnson, R. H., S. Chen, and J. J. Toth, 1989: Circulations associated with a mature-to-decaying midlatitude mesoscale convective system. Part I: Surface features—Heat bursts and mesolow development. *Mon. Wea. Rev.,* **117,** 942–959.

Keenan, T. D., and Coauthors, 1994: Science plan—Maritime Continent Thunderstorm Experiment. BMRC Research Rep. 44, 61 pp. [Available from BMRC, G.P.O. Box 1289K, Melbourne 3001, Victoria, Australia.]

——, K. Glasson, F. Cummings, T. Bird, J. Keeler, and J. Lutz, 1998: The BMRC/NCAR C-Band polarimetric (C-Pol) radar system. *J. Atmos. Oceanic Technol.,* **15,** 871–886.

Knupp, K. R., and W. R. Cotton, 1982: An intense, quasi-steady thunderstorm over mountainous terrain. Part II. Doppler radar observations of the storm morphological structure. *J. Atmos. Sci.,* **39,** 343–358.

Kuettner, J. P., P. A. Hildebrand, and T. L. Clark, 1987: Convection waves: Observations of gravity wave systems over convectively active boundary layers. *Quart. J. Roy. Meteor. Soc.,* **113,** 445–467.

Liu, C.-H., and M. W. Moncrieff, 1996a: A numerical study of the effects of ambient flow and shear on density currents. *Mon. Wea. Rev.,* **124,** 2282–2303.

——, and ——, 1996b: An analytical study of density currents in sheared, stratified fluids including the effects of latent heating. *J. Atmos. Sci.,* **53,** 3303–3312.

Mahoney, W. P., 1988: Gust front characteristics and the kinematics associated with interacting thunderstorm outflows. *Mon. Wea. Rev.,* **116,** 1474–1491.

Martner, B. E., 1997: Vertical velocities in a thunderstorm gust front and outflow. *J. Appl. Meteor.,* **36,** 615–622.

May, P. T., R. G. Strauch, K. P. Moran, and W. E. Ecklund, 1990: Temperature sounding by RASS with wind profiler radars: A preliminary study. *IEEE Trans. Geosci. Remote Sens.,* **28,** 19–28.

——, W. L. Ecklund, and G. D. Hess, 1995: Spectral and bispectral characteristics of wind variability at Darwin, Australia measured by a 50 MHz radar wind profiler. *Quart. J. Roy. Meteor. Soc.,* **121,** 527–544.

Mueller, C. K., and R. E. Carbone, 1987: Dynamics of a thunderstorm outflow. *J. Atmos. Sci.,* **44,** 1879–1898.

Passarelli, R. E., P. Romanik, S. G. Geotis, and A. D. Siggia, 1981: Ground clutter rejection in the frequency domain. Preprints, *20th Conf. on Radar Meteorology,* Boston, MA, Amer. Meteor. Soc., 295–300.

Rotunno, R., J. B. Klemp, and M. L. Weisman, 1988: A theory for strong, long-lived squall lines. *J. Atmos. Sci.,* **45,** 463–485.

Seitter, K. L., 1986: A numerical study of atmospheric density current motion including the effect of condensation. *J. Atmos. Sci.,* **43,** 3068–3076.

——, and H. S. Muench, 1985: Observation of a cold front with rope cloud. *Mon. Wea. Rev.,* **113,** 840–848.

Shapiro, M. A., T. Hampel, D. Rotzoll, and F. Mosher, 1985: The frontal hydraulic head: A micro-α scale ($\sim$1 km) triggering mechanism for mesoconvective weather systems. *Mon. Wea. Rev.,* **113,** 1166–1183.

Simpson, J. E., 1969: A comparison between laboratory and atmospheric density currents. *Quart. J. Roy. Meteor. Soc.,* **95,** 758–765.

——, and R. E. Britter, 1980: A laboratory model of an atmospheric mesofront. *Quart. J. Roy. Meteor. Soc.,* **106,** 485–500.

Thorpe, A. J., M. J. Miller, and M. W. Moncrieff, 1982: Two-dimensional convection in non-constant shear: A model of midlatitude squall lines. *Quart. J. Roy. Meteor. Soc.,* **108,** 739–762.

Wakimoto, R. M., 1982: The life cycle of thunderstorm gust fronts as viewed with Doppler radar and rawinsonde data. *Mon. Wea. Rev.,* **110,** 1060–1082.

Weckworth, T. M., and R. M. Wakimoto, 1992: The initiation and organization of convective cells atop a cold-air outflow boundary. *Mon. Wea. Rev.,* **120,** 2169–2187.

Wilson, J. W., and W. E. Schreiber, 1986: Initiation of convective storms at radar observed boundary-layer convergence lines. *Mon. Wea. Rev.,* **114,** 2516–2536.

——, T. D. Keenan, and R. E. Carbone, 1997: Hector initiation: Is it a breeze? Preprints, *28th Conf. on Radar Meteorology,* Austin, TX, Amer. Meteor. Soc., 567–568.